Near-infrared nanospectroscopy using a low-noise supercontinuum source

Kaltenecker, Korbinian J.; Rao D. S., Shreesha; Rasmussen, Mattias; Lassen, Henrik B.; Kelleher, Edmund J.R.; Krauss, Enno; Hecht, Bert; Mortensen, N. Asger; Grüner-Nielsen, Lars; Markos, Christos

Total number of authors:
13

Published in:
APL Photonics

Link to article, DOI:
10.1063/5.0050446

Publication date:
2021

Document Version
Publisher's PDF, also known as Version of record

APL Photonics

Near-infrared nanospectroscopy using a low-noise supercontinuum source

Cite as: APL Photonics **6**, 066106 (2021); https://doi.org/10.1063/5.0050446
Submitted: 15 March 2021 • Accepted: 25 May 2021 • Published Online: 15 June 2021

Korbinian J. Kaltenecker, Shreesha Rao D. S., Mattias Rasmussen, et al.

Near-infrared nanospectroscopy using a low-noise supercontinuum source

Cite as: APL Photon. 6, 066106 (2021); doi: 10.1063/5.0050446
Submitted: 15 March 2021 • Accepted: 25 May 2021 •
Published Online: 15 June 2021

Korbinian J. Kaltenecker,[1,2,a] Shreesha Rao D. S.,[1] Mattias Rasmussen,[1] Henrik B. Lassen,[1] Edmund J. R. Kelleher,[1] Enno Krauss,[3] Bert Hecht,[3] N. Asger Mortensen,[2,4,5] Lars Grüner-Nielsen,[1] Christos Markos,[1] Ole Bang,[1,6] Nicolas Stenger,[1,2,7] and Peter Uhd Jepsen[1,2,b]

AFFILIATIONS

[1] DTU Fotonik - Department of Photonics Engineering, Technical University of Denmark, DK-2800 Kongens Lyngby, Denmark
[2] Center for Nanostructured Graphene, Technical University of Denmark, DK-2800 Kongens Lyngby, Denmark
[3] Nano-Optics and Biophotonics Group, Experimentelle Physik 5, Physikalisches Institut, Universität Würzburg, D-97074 Würzburg, Germany
[4] Center for Nano Optics, University of Southern Denmark, DK-5230 Odense M, Denmark
[5] Danish Institute for Advanced Study, University of Southern Denmark, DK-5230 Odense M, Denmark
[6] NKT Photonics A/S, Blokken 84, 3460 Birkerød, Denmark
[7] NanoPhoton–Center for Nanophotonics, Technical University of Denmark, 2800 Kgs. Lyngby, Denmark

[a] **Present address:** Fakultät für Physik and Center for Nanoscience (CeNS), Ludwig-Maximilians-Universität, 80539 München, Germany.
[b] **Author to whom correspondence should be addressed:** puje@fotonik.dtu.dk

ABSTRACT

Unlocking the true potential of optical spectroscopy on the nanoscale requires development of stable and low-noise laser sources. Here, we have developed a low-noise supercontinuum (SC) source based on an all-normal dispersion fiber pumped by a femtosecond fiber laser and demonstrate high resolution, spectrally resolved near-field measurements in the near-infrared (NIR) region. Specifically, we explore the reduced-noise requirements for aperture-less scattering-type scanning near-field optical microscopy (s-SNOM), including inherent pulse-to-pulse fluctuation of the SC. We use our SC light source to demonstrate the first NIR, spectrally resolved s-SNOM measurement, a situation where state-of-the-art commercial SC sources are too noisy to be useful. We map the propagation of surface plasmon polariton (SPP) waves on monocrystalline gold platelets in the wavelength region of 1.34–1.75 μm in a single measurement, thereby characterizing experimentally the dispersion curve of the SPP in the NIR. Our results represent a technological breakthrough that has the potential to enable a wide range of new applications of low-noise SC sources in near-field studies.

I. INTRODUCTION

Today's silica fiber-based supercontinuum (SC) sources are ultra-broadband spatially coherent lasers covering several octaves from the visible (400 nm) to the near-infrared (NIR) (2400 nm) with a brightness that is over seven orders of magnitude higher than that of a Globar and even 2–3 orders of magnitude higher than that of a synchrotron.[1] Using SC generation in gas-filled hollow-core fibers, the spectrum is being extended to the vacuum UV below 113 nm,[2] and using chalcogenide fibers, the spectrum is being pushed to the mid-IR above 13 μm.[3] In many ways, the SC source resembles an ultra-bright table-top synchrotron with a tremendous range of applications.

In this paper, we demonstrate the leap in the performance of our newly developed low-noise SC source compared to existing commercial SC sources by spectroscopic imaging of surface plasmon polariton (SPP) waves propagating at the interface of extremely flat monocrystalline gold platelets. The broadband and ultra-quiet nature of the SC source, together with interferometric measurement techniques, allows us to measure the experimental

dispersion curve over the range 1.34–1.75 μm of the SPP waves.

A. All-normal dispersion supercontinuum generation

There has been a recent push toward understanding and suppressing the noise of SC sources due to the increasing number of applications within spectroscopy and a wide range of imaging modalities, such as ultra-high resolution spectral domain optical coherence tomography (OCT),[4,5] spectroscopic optical resolution photo-acoustic microscopy (OR-PAM),[6,7] scanning confocal fluorescence microscopy,[8,9] and flow cytometry.[10] Commercially available and high-average power SC sources are all based on pumping a nonlinear optical fiber in the anomalous dispersion regime close to the zero-dispersion wavelength with long picosecond (ps) and nanosecond (ns) pulses. This means that the SC generation is initiated by modulational instability (MI) growing from noise and breaking up the pump pulse into hundreds of solitons.[11–13] Consequently, the SC sources are inherently noisy,[13] which reduces the quality and resolution of images as well as the detection limit that can be obtained with spectroscopy using the SC source. Fundamental processes, such as soliton spectral alignment, can somewhat lower the noise of such MI- and soliton-based SC sources,[14,15] and the SC sources can be repetition rate doubled several times to increase the averaging of the detectors in the imaging systems.[16,17] However, such approaches have only reduced the noise by a factor of up to four.

One of the most promising approaches to reduce the noise by orders of magnitude is to generate the SC in a fiber with weak all-normal dispersion (ANDi) using ultra-short femtosecond (fs) pump pulses, in which case the spectral broadening can be dominated by the coherent processes of self-phase modulation (SPM) and optical wave-breaking (OWB).[18–20] Here, a first critical obstacle to low-noise performance is that the normal dispersion is weak in order to avoid parametric Raman noise.[21] Other key requirements to avoid Raman noise are that the pulse length and fiber length are sufficiently short and the pump peak power is sufficiently low.[21] Recent polarization and pump noise studies have also demonstrated that, in addition, the pump peak power and amplitude noise need to be low enough and the fiber birefringence needs to be high enough to avoid detrimental noise from polarization MI (PMI).[22,23] While several limiting requirements have thus been pointed out, these are still possible to satisfy, and the ultra-low-noise regime of an ANDi SC source is, therefore, realistically achievable.

B. Supercontinuum light sources and near-field microscopy

An important application where low noise of an SC source is of critical importance is scattering-type scanning near-field optical microscopy (s-SNOM).[24] s-SNOM is based on scattering of an incident optical field by a metallic tip sharpened to a tip radius of a few tens of nanometers, typically implemented as a modified atomic force microscope (AFM) with optical access. The scattering cross section of the tip depends on the local dielectric constant immediately under the tip, and therefore, the spatial resolution is determined by the radius of curvature of the tip and not by wavelength-dependent diffractive focusing of the incident optical field. This sensitivity to the local environment comes from the plasmonic-driven concentration of the incident field at the apex of the tip. The field concentration depends on image-charge effects at the surface of the material under the tip. Hence, the local field under the tip depends nonlinearly on the distance between the tip and the surface. In order to detect the near-field contribution to the total scattered field, the tip is tapped in and out of the near-field zone, and the near-field contribution to the scattered light intensity is recovered by demodulation at a harmonic $n \times \Omega$ of the tapping frequency Ω.[25,26] The spectrally resolved amplitude and phase of the scattered field can be acquired by asymmetric Fourier transform spectroscopy,[27] where the tip is located in the static arm of an asymmetric Michelson interferometer.[28,29] Since the photodetector measuring the back-scattered light receives the full scattered light field, source noise will inevitably have a large impact on the quality of the recovered high-order demodulated near-field signal. As an alternative to the aperture-less s-SNOM technique, aperture-based methods typically rely on an optical fiber tapered to nanometer dimensions and coated with metal.[30,31] The aperture can, in this manner, be reduced to less than 100 nm—deeply sub-wavelength relative to the wavelength of the incident field. The near field of a transilluminated sample is collected by the aperture, which, due to its sub-wavelength diameter, offers a small but measurable signal. Scanning of the fiber tip across the sample can, in this manner, reveal the local optical properties of materials.

Near-field spectroscopic imaging has been pursued intensively in the past couple of decades using incoherent light sources as well as coherent synchrotron and laser-based light as illumination sources. As an example of the use of an incoherent light source, Aigouy *et al.*[32] used a monochromatized xenon lamp coupled into an optical fiber for delivery and detected the scattered signal from an AFM tip with an apex diameter of ~100 nm. In this manner, wavelength-dependent scattering spectra (in the range 400–600 nm) from gold islands, recorded at the tapping frequency of the AFM tip, were reported and compared to far-field results. Bechtel *et al.*[33] used mid-IR radiation from a synchrotron (700–5000 cm^{-1} corresponding to 2–14 μm) for <40 nm spatial resolution imaging of semiconductors, biominerals, and protein nanostructures. The high brightness compared to an incoherent light source resulted in very high signal-to-noise contrast of the recorded images and allowed interferometric detection of the broad spectrum of the scattered light. Less expensive and more versatile ways to generate broadband light with low noise for near-field spectroscopy have also been explored. A few examples include the use of tunable laser sources in the mid-infrared for spectroscopic near-field imaging of, for instance, nanoparticles of PMMA and cylindrical tobacco viruses[34] and plasmon–phonon interactions in highly doped graphene.[35] There are, however, significant advantages in using broadband light sources for near-field studies. This has motivated efforts to apply SC-based light sources in near-field experiments. Notably, Nagahara *et al.*[36] used aperture-based SNOM with an SC generated in a nonlinear photonic crystal fiber (PCF) pumped by a Ti:sapphire fs laser for optical pump–probe near-field measurements with ps time resolution. Spectral resolution was obtained by slicing of the wavelengths of the SC with tunable filters. Mikhailovsky *et al.*[37] used a fs white-light continuum generated in a sapphire plate and transmitted through a sub-wavelength aperture of a tapered fiber for the study of surface plasmon resonances in gold nanoparticles and their dimers. Bakker *et al.*[38] used a compact SC light source based on a Nd:YAG pulsed microchip laser pumping a PCF at 1064 nm, with 550–950 nm spectral coverage, and obtained

sub-wavelength resolution with a cantilever-mounted tapered fiber probe with 150 nm aperture. Dvořák *et al.*[39] used a commercially available SC source (Fianium) for non-interferometric near-field mapping of surface plasmon polaritons on gold structures deposited on quartz. The SNOM was aperture-based, with an aperture opening of 50 nm, and the study was performed with wavelength selection before the imaging. The whole sample was illuminated, and the local light intensity was picked up by the probe tip. Experimental interference patterns (in the range of 550–750 nm) of surface plasmon polaritons (SPPs) propagating in different directions on a square sample of dimensions ~10 × 10 μm^2 were observed, and the SPP dispersion curves across the visible spectral range could be extracted from the images.

A series of papers from various authors have used difference-frequency generation (DFG) in the mid-infrared for broadband, wavelength-tunable s-SNOM studies. The technique, first developed for near-field imaging by Keilmann and Amarie[40] based on previous developments by Gambetta *et al.*,[41] uses a fs Er:fiber laser, where a part of the beam is turned into an SC spanning of 0.9–2.2 μm. The long-wavelength portion of the SC is mixed with residual pump light in a GaSe nonlinear optical crystal, phase-matched for DFG in the mid-infrared. This source was first applied for the investigations of phonons in silicon carbide (SiC)[42] and has been applied, for instance, to map the optical properties of optical phonons in the mid-infrared[43,44] and the dynamics of photoexcited charge carriers in InAs.[45] These light sources in combination with s-SNOM have been used to map the propagation of phonon polaritons with hyperbolic dispersion[43] as well as their resonance modes in confined structures[46] with lateral spatial resolution better than 20 nm. The combination of s-SNOM with broadband light sources featuring low noise is thereby a powerful tool to explore the fundamental properties of light-matter interactions in the near-field on the nanometer scale.

In spite of the apparent advantages of SC-based light sources for s-SNOM, there is limited quantitative information available in the literature about their noise properties. In this paper, we demonstrate that when applied to near-field interferometric s-SNOM, an ANDi-based SC source shows performance comparable to that of a low-noise passively mode-locked fs laser but offering a greatly enhanced spectral bandwidth enabling broadband spectroscopy in a single measurement, without tuning the wavelength of the source. In contrast, we highlight that standard commercial SC sources are severely limited with regard to their application in s-SNOM measurements due to their high intrinsic noise. We critically evaluate the SC noise, with particular attention paid to the indicators relevant for sensitive near-field studies, benchmarking the performance against the commercial SC system. Targeting a region of the near-infrared (NIR) from 1.4 to 1.8 μm is important for a number of key research areas, not least because it covers the full telecommunication window. We emphasize that our advancement is distinct both technologically and application-wise from earlier work with SC sources in the mid-infrared.

II. MATERIALS AND METHODS

We compare the performance of two broadband SC sources and a fs laser for s-SNOM in the NIR using a commercial s-SNOM spectrometer (neaSNOM, attocube) with an FTIR unit (nano-FTIR, attocube) equipped with a fused silica beam splitter (600–1700 nm). We used Arrow NCPt AFM tips (NanoWorld) for the measurements. In all experiments reported here, we used an average optical power of 2–3 mW to drive the s-SNOM. The full setup is shown in Fig. 1. The first SC source is a commercially available 20 MHz SuperK Extreme (NKT Photonics), which covers the wavelength range from 0.39 to 2.40 μm. The output spectrum of this source has a strong peak at the pump wavelength (1064 nm), which is why we remove the short-wavelength part of the spectrum (<1.30 μm) using a long-pass filter. We compare the performance of this SC source with our low-noise ANDi SC source covering the wavelength range from 1.34 to 1.75 μm (5550–7300 cm^{-1} and a useful bandwidth of 1750 cm^{-1})[47] and a commercial fs laser (Toptica Er:fiber; a central wavelength of 1550 nm, a pulse duration of 125 fs, a repetition rate of 90 MHz, and an average power of 280 mW). The ANDi fiber (OFS

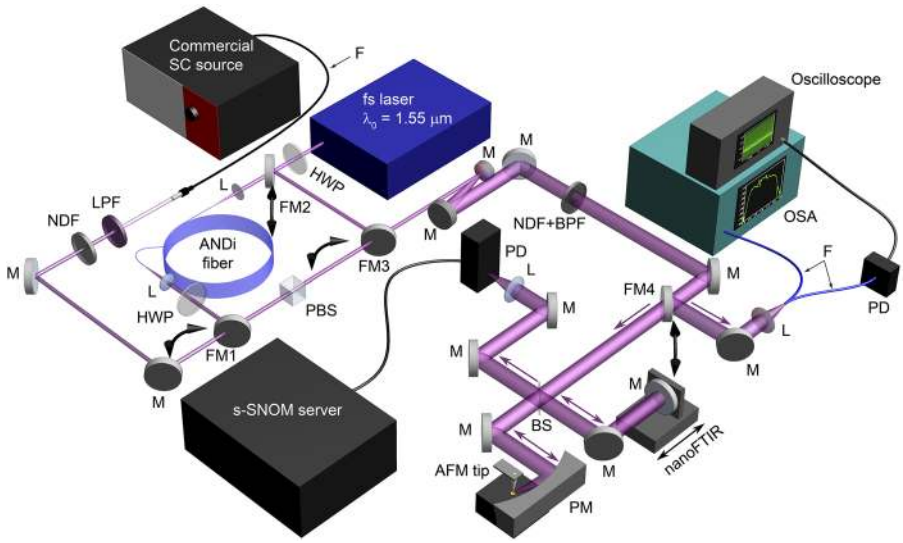

FIG. 1. Sketch of the setup (M = mirror, FM = flip mirror, LPF = long-pass filter, NDF = neutral density filter, BPF = bandpass filter, F = optical fiber, HWP = half-wave plate, L = lens, PBS = polarizing beam splitter, PM = parabolic mirror, PD = photodetector, and OSA = optical signal analyzer).

Denmark) is pumped by the same fs Er:fiber laser. Details on the ANDi fiber and its characterization are given in the supplementary material.

The useful bandwidth of the ANDi SC is determined by the region of low, normal dispersion of the fiber used for SC generation.[47] By using the same fs laser for ANDi and reference measurements, we can directly measure additional noise from the SC generation and compare it to the noise of the pump laser. By using flip mirrors (FMs), either the low-noise SC beam (via FM1) or the beam of the fs laser (via FM2 and 3) can be coupled into the optical setup. The required vertical polarization and optimal spectrum are ensured by the combination of a broadband half-wave plate (HWP) and polarizing beam splitter (PBS). After passing through a common beam expander, the chosen beam from one of the three sources can either be sent into the s-SNOM system or be coupled into a fiber via FM4 for direct characterization of the properties of the input beam. The collection fiber (core diameter of 50 μm) can be connected to an optical spectrum analyzer (OSA, Yokogawa AQ6375) to measure the input spectrum or an InGaAs photodetector (Thorlabs DET08CFC, 5 GHz bandwidth, 80 μm active area diameter) and real-time oscilloscope (Teledyne LeCroy HDO9404, 4 GHz bandwidth, 40 GS/s) to determine the relative intensity noise (RIN), which is a standard figure-of-merit of the pulse-to-pulse fluctuation in intensity of a pulsed laser, based on statistics extracted from a long time-series record of many thousands of individual pulses.

III. RESULTS AND DISCUSSION

A. Hyper-spectral nano-imaging of surface plasmon polaritons on monocrystalline gold platelets

We use our low-noise ANDi-based SC source to measure interference fringes of SPPs on high-quality monocrystalline gold platelets. It was recently shown that the measurement of SPPs on a gold film with s-SNOM leads to rich and complex distributions of the scattering signal due to the contributions of several excitation and detection channels,[48,49] thus representing a challenging case for our developed setup. Figure 2 shows the excitation geometry of the s-SNOM tip and the gold platelet. The image of the gold platelet is the topology map recorded by the s-SNOM. There are two possible excitation and detection channels that are relevant for this experiment. The first SPP related pathway shown in Fig. 2(a) is due to tip-launched SPPs, i.e., the incident beam excites SPPs at the tip, which radially propagate away from the tip. If the propagation direction of the SPPs is perpendicular to the edge, they will be partially reflected back toward the tip. The outgoing and incoming SPPs interfere at the tip, and when scanning the tip along a line that is perpendicular to the edge [gray dashed line in both Figs. 2(a) and 2(b) but best seen in (b)], the scattered signal forms a field pattern that is similar to a standing wave with a fringe spacing of $\Lambda_{tl} = \lambda_{spp}/2$, where λ_{spp} is the SPP wavelength.[50] The second SPP related excitation and detection channel is illustrated in Fig. 2(b). The incident beam that is focused on the tip has, due to the diffraction limit, a finite diameter. Because of the shallow incident angle of $\vartheta = 60°$, the spot size is ~5 μm perpendicular to and 21 μm in the direction of the projection of the incident beam on the sample surface. If a part of the beam hits the edge, SPPs can be excited, which eventually propagate toward the tip. These waves can, to a good approximation, be described by plane waves in contrast to the circular waves launched by the tip. When they reach the tip, they can be scattered and additional fringes are formed due to the interference between the edge-launched SPPs and the in-plane component of the incident laser beam.[51] In addition, here, a typical fringe spacing is obtained when the tip is scanned along a line perpendicular to the edge, which is given by[49]

$$\Lambda_{el} = \frac{\lambda_0}{-\sin(\vartheta)\sin(\varphi) + \sqrt{\sin^2(\vartheta)\sin^2(\varphi) - \sin^2(\vartheta) + n_{eff}^2}}, \quad (1)$$

where λ_0 is the wavelength of the incident light, ϑ is the incident angle, φ is the azimuth angle of the beam with respect to the edge, and n_{eff} is the effective refractive index at the gold interface and is related to the theoretical dispersion relation of the SPPs by $n_{eff} = \mathrm{Re}[\tilde{\beta}/k_0]$, where $\tilde{\beta} = \sqrt{\tilde{\epsilon}/(1+\tilde{\epsilon})}$ is the complex-valued wave vector of the SPPs propagating at the surface of a metal with

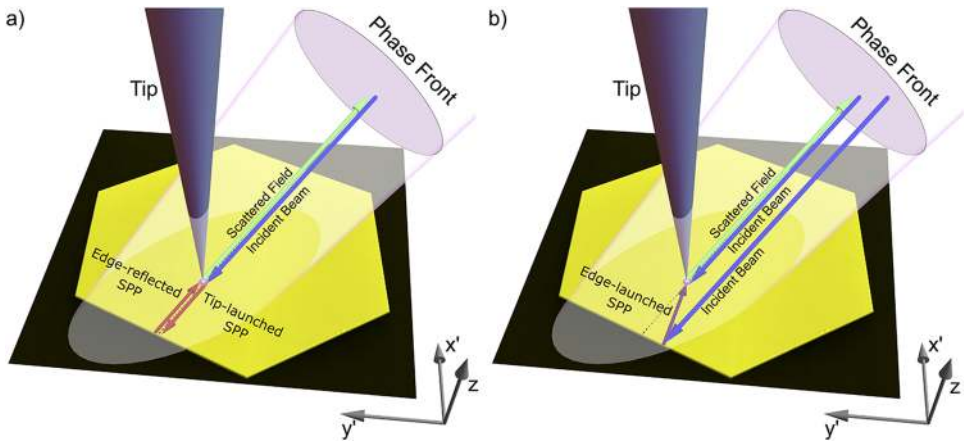

FIG. 2. Excitation and detection paths of SPPs on monocrystalline gold platelets with s-SNOM: (a) tip-launched SPPs and (b) edge-launched SPPs. The gold flake image is based on a topology map recorded by the s-SNOM system.

complex dielectric constant $\tilde{\varepsilon}$. When a part of the beam illuminates the edge, both channels will contribute to the measured signal simultaneously. Edge-launched SPPs, however, are more dominant than tip-launched SPPs. The resulting field pattern is thus a superposition of fringes due to the edge-launched SPPs described by a plane wave and tip-launched SPPs described by a cylindrical wave.

We formed an average of eight consecutive line scan measurements from the edge toward the center of the gold platelet, as indicated by the gray dashed line in Fig. 2, recording the spectra with the nano-FTIR unit at 300 pixels along the line. The azimuth angle was set to $\varphi = 67°$. We then calculated the average of the seven measurements for each pixel. Each interferogram consists of 700 data points over 140 μm movement of the interferometer arm. With an integration time of 17 ms per step, the total data acquisition time for the data shown in Fig. 3 was ~7 h.

The resulting map of the scattering amplitude $|S_3(\lambda_0, x)|$ for all incident wavelengths λ_0 within the bandwidth of the SC pulses is shown in Fig. 3(a). For clarity, we normalized the profiles at each wavelength. For each wavelength, we obtain a periodic pattern where the spacing of the fringe maxima increases for a longer illumination wavelength. The black dotted lines are separated along the x axis by the theoretical value of the fringe spacing for edge-launched SPPs for the respective illumination wavelength λ_0, which is in good agreement with the measurement. The signal profile at $\lambda_0 = 1.6$ μm (blue dashed line) is shown as an example in Fig. 3(c). In a next step, we perform a discrete Fourier transformation (FFT) over the entire x-range of Fig. 3(a), which is also marked in Fig. 3(c) by the two red vertical lines, to obtain the fringe spacings from the resulting spatial frequency spectra $S_3(\lambda_0, K) = \mathcal{F}[|S_3(\lambda_0, x)|]$. The result of the FFT is shown in Fig. 3(b). We find maxima whose K values decrease

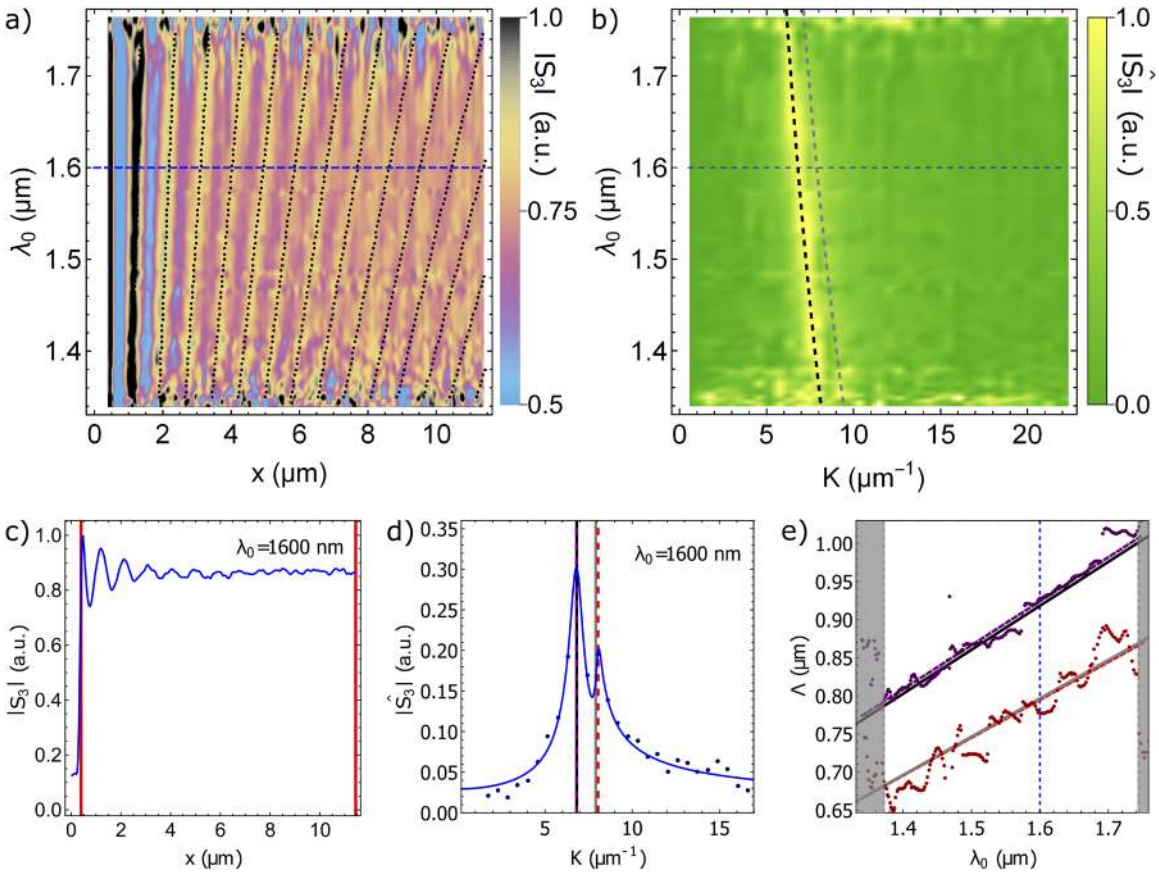

FIG. 3. Results of the experimental line scan from the edge to the center of the gold platelet. (a) Density plot of the scattering amplitude $|S_3(\lambda_0, x)|$ for different illumination wavelengths λ_0. The black dots mark the calculated fringe spacing of edge-launched SPPs at different illumination wavelengths. (b) Spatial frequency map by applying a FFT to the scattering amplitude $|S_3(\lambda_0, x)|$ in (a) at each illumination wavelength. The black and gray dashed curves correspond to the theoretical predictions of the spatial frequencies of edge-launched and tip-launched SPPs, respectively, and the blue dashed line marks the spatial frequency spectrum shown in (d). (c) Intensity profile of the near-field signal taken at the horizontal blue dashed line in (a). (d) Amplitude spectrum as a function of the spatial frequency K. The blue dots correspond to the Fourier-transformed experimental data taken between the two red vertical lines in (c). The blue curve is the result of the fitting procedure detailed in the main text. The black and gray vertical lines mark the theoretical values Λ_{el} and Λ_{tl}, respectively, and the purple and red lines show the two peak positions of the fit (partly overlapping with the black and gray lines due to the close agreement). (e) Resulting fringe spacings (purple and red dots) $\Lambda = 2\pi/K_{el,tl}$ for all illumination wavelengths and linear fits (purple and red dashed lines). The gray and black lines correspond to theoretical values of $\Lambda = 2\pi/K_{el,tl}$ in the wavelength range of the SC source, respectively. The gray shaded areas indicate ranges where noise dominates.

with increasing illumination wavelength. The theoretical values $K_{el} = 2\pi/\Lambda_{el}$ of edge-launched SPPs (black dashed curve) overlap well with our measured data. Furthermore, we find an increase in the signal on the right shoulder of the main peak, where the theoretical spatial frequency value $K_{tl} = 2\pi/\Lambda_{tl}$ of the tip-launched SPPs is located (gray dashed curve). This becomes more apparent in Fig. 3(d), which shows the corresponding spatial frequency spectrum at $\lambda_0 = 1.6\ \mu$m. The theoretical prediction of the K values for edge-launched and tip-launched SPPs is marked by the black and gray vertical lines, respectively. To identify the position of these two peaks (labeled 1 and 2) in the data, we perform simultaneously a fit with the absolute value of the Fourier transform $|\mathcal{F}[f_1(x) + f_2(x)]|$ of a cylindrical wave $f_1(x) = A_1\Theta(x)\cos(K_1x)\exp(-\Gamma_1x)/\sqrt{2x}$ and a plane wave $f_2(x) = A_2\Theta(x)\cos(K_2x)\exp(-\Gamma_2x)$, where $\Theta(x)$ is the Heaviside step function. $\Gamma_{1,2}$ and $K_{1,2}$ are the decay parameter and the spatial frequency vector of the obtained field distribution of fringes due to tip-launched and edge-launched SPPs, respectively. The resulting fit is shown by the blue curve, while the purple and red vertical lines mark the fitted peak positions, which are in good agreement with the positions of the black and gray vertical lines obtained theoretically. We apply our fitting procedure to all illumination wavelengths and plot in Fig. 3(e) the fitted peak positions (purple and red dots) in terms of fringe spacing $\Lambda = 2\pi/K$ as a function of the illumination wavelength. The fitted fringe spacings, which are related to the first peak in the spatial frequency spectra (purple dots), are closely located to the theoretical prediction of the fringe spacing of edge-launched SPPs indicated by the black curve. The fringe spacings, which are related to the second peak in the spatial frequency spectra, are distributed around the predicted values for tip-launched SPPs (gray curve). The gray dashed vertical lines mark the wavelength range in which the signal is reliable enough to perform the fit with confidence. As a last step, we make a linear fit through the purple and red dots, respectively, which are plotted as purple and red dashed lines. Both linear fits are in good agreement with the theoretical predictions for edge-launched and tip-launched SPPs, respectively. These results convincingly demonstrate the versatility of the ANDi SC source operating in the NIR wavelength region for broadband s-SNOM based nanospectroscopy.

B. Relative intensity noise (RIN) and s-SNOM performance

To characterize the spectrally resolved RIN of the different sources, we used 12 nm bandpass filters (at 50 nm intervals) and

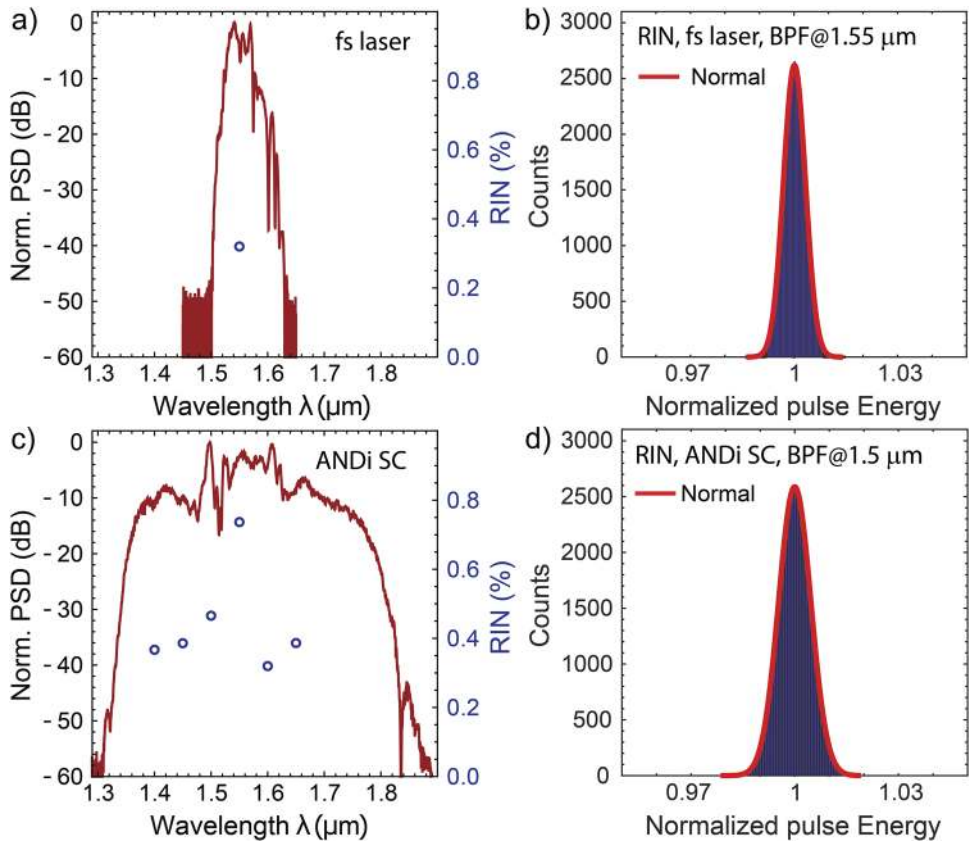

FIG. 4. (a) Toptica 1.55 μm fs laser spectrum (red) and RIN of the 12 nm filtered signal at 1.55 μm (blue point). (b) Pulse energy distribution of the 12 nm filtered signal at 1.55 μm. (c) Low-noise ANDi SC spectrum (red) and spectrally resolved RIN at 1.4–1.65 μm (blue dots). (d) Pulse energy distribution recorded with a 12-nm BPF at 1.50 μm.

detected time series of the filtered spectrum by the fast photodetector and real-time sampling oscilloscope. The RIN was then defined from the statistics as the standard deviation divided by the mean. In general, the recorded statistical distribution of an SC source depends on the wavelength and can vary from being Gaussian shaped (typically close to the pump) to strongly L-shaped (typically close to the edges).[52] The details of the RIN measurement procedure are described in the supplementary material. This technique for measuring RIN has been applied in several earlier works on SC noise.[47,53] To understand the contribution of the pump laser to the overall noise of the ANDi SC source, the optical spectrum and corresponding RIN of the 125 fs, 1550 nm pump laser were first measured directly before the SC generation and are shown in Fig. 4(a). The spectrum extends over 130 nm (from 1.50 to 1.63 μm). RIN measurements were performed in a 12 nm band at a center wavelength of 1.55 μm. The measured RIN was found to be 0.36%, and the pulse energy distribution of the recorded pulses was close to Gaussian, as shown in Fig. 4(b). We note that the measured RIN of the pump was reported to be 1% in Ref. 47 in which case the laser was optimized for maximum average power out of the laser. In this case, the same laser was thoroughly optimized for minimum pulse-to-pulse fluctuation, and a low-RIN of 0.36% was obtained after the optimization. The measured spectrum and spectrally resolved RIN (in the wavelength range of 1.4–1.65 μm) of the ANDi SC source is shown in Fig. 4(c), and an example of the approximately Gaussian distribution of the pulse energy distribution of the recorded pulses is shown in Fig. 4(d). The RIN remains below 0.7% across the measured bandwidth, which supports the fact that the spectrum broadens deterministically by SPM and OWB. Furthermore, the ANDi SC shows only a slight increase in the RIN in comparison to the pump laser itself at the pump wavelength and shows the same RIN level as the pump laser outside the pump wavelength region.

In contrast, the reference SC source has a markedly higher RIN. As detailed in the supplementary material, we find a spectrally averaged RIN of 4.7% across the 1.3–1.8 μm range and a spectrally resolved RIN that shows an increase from 16% at 1.35 μm to 28% at 1.65 μm. Our detailed RIN measurements thus confirm that the noise of the commercial SuperK source across the bandwidth is more than 23 times higher than that of the ANDi source. We anticipate this to have serious implications for the performance of the

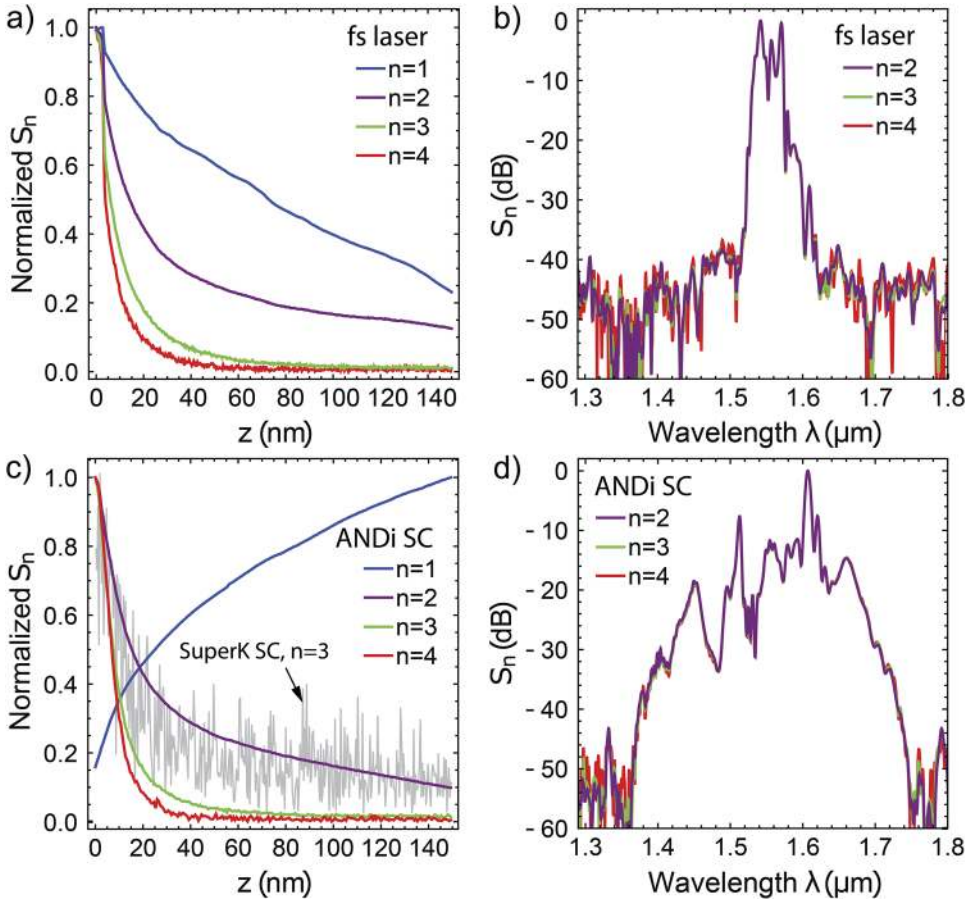

FIG. 5. (a) Approach curves of the s-SNOM system driven by the Toptica fs laser, recorded at demodulation orders $n = 1, 2, 3, 4$ and (b) interferometric (nano-FTIR) measurement of the Toptica fs laser spectrum ($n = 2, 3, 4$). (c) and (d) Same as (a) and (b) but recorded with the full ANDi spectrum.

s-SNOM system, as we will now consider. With the s-SNOM system, we recorded the approach curves (scattered signal from the tip as a function of the tip-surface distance) using the same monocrystalline gold platelet sample as above[48] [see Figs. 5(a) and 5(c)]. This measurement allows us to determine the noise level of the different demodulation orders (n) and the contribution of the near-field in the demodulated signal channels (S_n) of the reference SC source, the ANDi SC source, and the fs laser driving the ANDi SC. In a second step, we recorded the spectrum of the scattered near-field signal along a scan line on the sample surface with an asymmetric Fourier transform[27] spectrometer (nanoFTIR unit from attocube/Neaspec[28,29]) integrated in our s-SNOM system. Representative spectra are shown in Figs. 5(b) and 5(d) for the fs laser and ANDi source, respectively, and in the supplementary material for the reference SC source. Interferometric techniques, such as nano-FTIR, allow for a further reduction of the background and a simultaneous measurement of the electric field amplitude and phase over the entire bandwidth of the illumination source.[54] In the experiments presented here, we were limited by the responsivity of our InGaAs photodetector to wavelengths in the range of 0.9–1.8 μm. We show results in the wavelength range of 1.3–1.8 μm covered by the ANDi SC source. Finally, we evaluated the performance of the low-noise ANDi SC source, whose noise is primarily dependent on the noise level of the pump laser[47] in connection with the spectrally resolved s-SNOM measurements. As with the RIN measurements, we compare directly with the performance of the low-noise fs pump laser. The stability of the fs laser is superior to the commercial SC source, which is reflected in the quality of the approach curves, as shown in Fig. 5(a). The noise level is orders of magnitude lower than observed for the reference SC source for all higher harmonics of the demodulated signal (see the supplementary material). The third and fourth demodulation orders satisfy the criterion for containing sufficient near-field contributions in the scattered signal (decay of the approach curve to below $1/e \approx 0.37$ in less than 20 nm). The spectra measured with the nano-FTIR unit of the s-SNOM reproduce the input spectrum [see Fig. 4(a)] well at all displayed demodulation orders ($n = 2, 3, 4$) with noise levels below 36 dB.

Based on the measured RIN of the ANDi SC source shown in Fig. 4(c), which has a level similar to the fs laser across its full bandwidth except for an elevated RIN observed around the pump wavelength, we expect similar performance in the s-SNOM system. As shown in Fig. 5(c), we indeed obtain smooth approach curves at all demodulation orders, with the third and fourth harmonics of the demodulated signal satisfying the near-field criteria. For comparison of the noise levels, the corresponding approach curve ($n = 3$) recorded with the reference SC broadband spectrum is shown as the gray curve in Fig. 5(c) (see the supplementary material for full details). The SuperK approach curve was measured with an integration time constant of 100 ms, whereas the ANDi SC approach curves were recorded with 25 ms integration time per data point. The nano-FTIR spectra shown in Fig. 5(d) of the ANDi SC source overlap at all demodulation orders ($n = 2, 3, 4$) and possess a similar noise floor. Compared to the reference SC source (see the supplementary material), this is a major improvement, demonstrating that our ANDi SC source is compatible with s-SNOM and enables broadband near-field spectroscopy in a single measurement.

IV. CONCLUSIONS

We have demonstrated near-infrared s-SNOM across the 1.3–1.8 μm wavelength range. Both localized and propagating plasmons at this wavelength are of high technological relevance for integrated photonics due to the high degree of confinement of the electromagnetic field, but excessive damping in nanostructured metals has traditionally been a significant hindrance for long propagation lengths as well as high-quality-factor plasmon resonances.[55] Low-loss plasmons in ultrathin metal films are key in the future development of truly nanoscale electro-optic modulators and sensors with voltage-tunable response.[56,57] Our low-noise SC source in combination with s-SNOM can be an important tool in further experimental investigations of surface plasmon polaritons in these promising metallic platforms since it becomes possible to map the dispersion relation of the plasmon within a single measurement with a few nanometer spatial resolution. The enabling technology is an in-house built supercontinuum system using an all-normal dispersion (ANDi) fiber-based supercontinuum source that, in contrast to conventional SC sources, enables low-noise spectroscopic measurements using the weak demodulated near-field signals extracted from the large background present in the illumination of an s-SNOM system. The performance demonstrated with our new system cannot be reached with existing state-of-the-art commercial SC sources. Specifically, we have demonstrated that the relative intensity noise (RIN) of our ANDi SC source is in the range of 0.3%–0.7% across its full bandwidth and is comparable to the RIN (0.36%) of the low-noise mode-locked fiber laser at 1.55 μm that pumps the ANDi fiber. With this unique light source, we are able to spectrally resolve the dispersion of surface plasmon polariton waves propagating on a monocrystalline gold surface. The spectrally resolved measurements make it possible to directly distinguish SPP waves launched at the edges of the gold surface from those launched at the tip of the spectrometer. The spectral range covered by the ANDi SC source is determined by the design and the transparency range of the fiber, as well as the peak power of the pump laser. Thus, it is possible to shift the useful spectral range and make the bandwidth broader.[58] We believe that the technology presented here will be an important part of the toolbox in nanophotonics, including the investigation of light–matter interactions on the nanometer scale at wavelengths relevant for applications in high speed communications,[59] dielectric metasurfaces,[60] and quantum information processing.[61]

SUPPLEMENTARY MATERIAL

In the supplementary material, we give detailed information about the all-normal dispersion (ANDi) supercontinuum generation and further details on the relative intensity noise (RIN) performance of the commercial supercontinuum light source in relation to the s-SNOM measurements.

ACKNOWLEDGMENTS

We acknowledge funding from European Union's Horizon 2020 research and innovation program under Marie Sklodowska-Curie Grant Agreement No. 722380 (the project SUPUVIR), the Center for Nanostructured Graphene sponsored by the Danish National Research Foundation (Project No. DNRF103), and VILLUM FONDEN (Grant No. 16498). N.S. acknowledges support

from VILLUM FONDEN (Grant No. 00028233) and from the Independent Research Fund Denmark—Natural Sciences (Project No. 0135-004038).

The authors declare no conflicts of interest.

DATA AVAILABILITY

The data that support the findings of this study are available from the corresponding author upon reasonable request.

REFERENCES

[1]C. R. Petersen, P. M. Moselund, L. Huot, L. Hooper, and O. Bang, "Towards a table-top synchrotron based on supercontinuum generation," Infrared Phys. Technol. **91**, 182–186 (2018).

[2]F. Belli, A. Abdolvand, W. Chang, J. C. Travers, and P. S. J. Russell, "Vacuum-ultraviolet to infrared supercontinuum in hydrogen-filled photonic crystal fiber," Optica **2**, 292–300 (2015).

[3]C. R. Petersen, U. Møller, I. Kubat, B. Zhou, S. Dupont, J. Ramsay, T. Benson, S. Sujecki, N. Abdel-Moneim, Z. Tang, D. Furniss, A. Seddon, and O. Bang, "Mid-infrared supercontinuum covering the 1.4–13.3 μm molecular fingerprint region using ultra-high NA chalcogenide step-index fibre," Nat. Photonics **8**, 830–834 (2014).

[4]I. Hartl, X. D. Li, C. Chudoba, R. K. Ghanta, T. H. Ko, J. G. Fujimoto, J. K. Ranka, and R. S. Windeler, "Ultrahigh-resolution optical coherence tomography using continuum generation in an air–silica microstructure optical fiber," Opt. Lett. **26**, 608–610 (2001).

[5]N. M. Israelsen, C. R. Petersen, A. Barh, D. Jain, M. Jensen, G. Hannesschläger, P. Tidemand-Lichtenberg, C. Pedersen, A. Podoleanu, and O. Bang, "Real-time high-resolution mid-infrared optical coherence tomography," Light: Sci. Appl. **8**, 11 (2019).

[6]Y. N. Billeh, M. Liu, and T. Buma, "Spectroscopic photoacoustic microscopy using a photonic crystal fiber supercontinuum source," Opt. Express **18**, 18519–18524 (2010).

[7]M. K. Dasa, C. Markos, M. Maria, C. R. Petersen, P. M. Moselund, and O. Bang, "High-pulse energy supercontinuum laser for high-resolution spectroscopic photoacoustic imaging of lipids in the 1650-1850 nm region," Biomed. Opt. Express **9**, 1762–1770 (2018).

[8]G. McConnell, "Confocal laser scanning fluorescence microscopy with a visible continuum source," Opt. Express **12**, 2844–2850 (2004).

[9]R. Borlinghaus, "The white confocal: Continuous spectral tuning in excitation and emission," in *Optical Fluorescence Microscopy: From the Spectral to the Nano Dimension*, edited by A. Diaspro (Springer-Verlag, Berlin, 2011), pp. 37–54.

[10]V. Kapoor, F. V. Subach, V. G. Kozlov, A. Grudinin, V. V. Verkhusha, and W. G. Telford, "New lasers for flow cytometry: Filling the gaps," Nat. Methods **4**, 678–679 (2007).

[11]J. M. Dudley and S. Coen, "Coherence properties of supercontinuum spectra generated in photonic crystal and tapered optical fibers," Opt. Lett. **27**, 1180–1182 (2002).

[12]J. M. Dudley, G. Genty, and S. Coen, "Supercontinuum generation in photonic crystal fiber," Rev. Mod. Phys. **78**, 1135–1184 (2006).

[13]U. Møller, S. T. Sørensen, C. Jakobsen, J. Johansen, P. M. Moselund, C. L. Thomsen, and O. Bang, "Power dependence of supercontinuum noise in uniform and tapered PCFs," Opt. Express **20**, 2851–2857 (2012).

[14]R. D. Engelsholm and O. Bang, "Supercontinuum noise reduction by fiber undertapering," Opt. Express **27**, 10320–10331 (2019).

[15]K. Kwarkye, M. Jensen, R. D. Engelsholm, M. K. Dasa, D. Jain, P. Bowen, P. M. Moselund, C. R. Petersen, and O. Bang, "In-amplifier and cascaded mid-infrared supercontinuum sources with low noise through gain-induced soliton spectral alignment," Sci. Rep. **10**, 8230 (2020).

[16]W. Yuan, J. Mavadia-Shukla, J. Xi, W. Liang, X. Yu, S. Yu, and X. Li, "Optimal operational conditions for supercontinuum-based ultrahigh-resolution endoscopic OCT imaging," Opt. Lett. **41**, 250–253 (2016).

[17]M. Maria, I. Bravo Gonzalo, T. Feuchter, M. Denninger, P. M. Moselund, L. Leick, O. Bang, and A. Podoleanu, "Q-switch-pumped supercontinuum for ultra-high resolution optical coherence tomography," Opt. Lett. **42**, 4744–4747 (2017).

[18]C. Finot, B. Kibler, L. Provost, and S. Wabnitz, "Beneficial impact of wave-breaking for coherent continuum formation in normally dispersive nonlinear fibers," J. Opt. Soc. Am. B **25**, 1938–1948 (2008).

[19]A. M. Heidt, "Pulse preserving flat-top supercontinuum generation in all-normal dispersion photonic crystal fibers," J. Opt. Soc. Am. B **27**, 550–559 (2010).

[20]J. Takayanagi and N. Nishizawa, "Generation of widely and flatly broadened, low-noise and high-coherence supercontinuum in all-fiber system," Jpn. J. Appl. Phys., Part 2 **45**, L441–L443 (2006).

[21]A. M. Heidt, J. S. Feehan, J. H. V. Price, and T. Feurer, "Limits of coherent supercontinuum generation in normal dispersion fibers," J. Opt. Soc. Am. B **34**, 764–775 (2017).

[22]I. Bravo Gonzalo, R. D. Engelsholm, M. P. Sørensen, and O. Bang, "Polarization noise places severe constraints on coherence of all-normal dispersion femtosecond supercontinuum generation," Sci. Rep. **8**, 6579 (2018).

[23]E. Genier, P. Bowen, T. Sylvestre, J. M. Dudley, P. Moselund, and O. Bang, "Amplitude noise and coherence degradation of femtosecond supercontinuum generation in all-normal-dispersion fibers," J. Opt. Soc. Am. B **36**, A161–A167 (2019).

[24]F. Keilmann and R. Hillenbrand, "Near-field microscopy by elastic light scattering from a tip," Philos. Trans. R. Soc., A **362**, 787–805 (2004).

[25]B. Knoll and F. Keilmann, "Enhanced dielectric contrast in scattering-type scanning near-field optical microscopy," Opt. Commun. **182**, 321–328 (2000).

[26]R. Hillenbrand and F. Keilmann, "Complex optical constants on a subwavelength scale," Phys. Rev. Lett. **85**, 3029–3032 (2000).

[27]T. J. Parker, "Dispersive Fourier transform spectroscopy," Contemp. Phys. **31**, 335–353 (1990).

[28]F. Huth, A. Govyadinov, S. Amarie, W. Nuansing, F. Keilmann, and R. Hillenbrand, "Nano-FTIR absorption spectroscopy of molecular fingerprints at 20 nm spatial resolution," Nano Lett. **12**, 3973–3978 (2012).

[29]F. Huth, M. Schnell, J. Wittborn, N. Ocelic, and R. Hillenbrand, "Infrared-spectroscopic nanoimaging with a thermal source," Nat. Mater. **10**, 352–356 (2011).

[30]D. W. Pohl, W. Denk, and M. Lanz, "Optical stethoscopy: Image recording with resolution $\lambda/20$," Appl. Phys. Lett. **44**, 651–653 (1984).

[31]U. Dürig, D. W. Pohl, and F. Rohner, "Near-field optical-scanning microscopy," J. Appl. Phys. **59**, 3318–3327 (1986).

[32]L. Aigouy, F. X. Andréani, A. C. Boccara, J. C. Rivoal, J. A. Porto, R. Carminati, J.-J. Greffet, and R. Mégy, "Near-field optical spectroscopy using an incoherent light source," Appl. Phys. Lett. **76**, 397–399 (2000).

[33]H. A. Bechtel, E. A. Muller, R. L. Olmon, M. C. Martin, and M. B. Raschke, "Ultrabroadband infrared nanospectroscopic imaging," Proc. Natl. Acad. Sci. U. S. A. **111**, 7191–7196 (2014).

[34]M. Brehm, T. Taubner, R. Hillenbrand, and F. Keilmann, "Infrared spectroscopic mapping of single nanoparticles and viruses at nanoscale resolution," Nano Lett. **6**, 1307–1310 (2006).

[35]F. J. Bezares, A. D. Sanctis, J. R. M. Saavedra, A. Woessner, P. Alonso-González, I. Amenabar, J. Chen, T. H. Bointon, S. Dai, M. M. Fogler, D. N. Basov, R. Hillenbrand, M. F. Craciun, F. J. García de Abajo, S. Russo, and F. H. L. Koppens, "Intrinsic plasmon–phonon interactions in highly doped graphene: A near-field imaging study," Nano Lett. **17**, 5908–5913 (2017).

[36]T. Nagahara, K. Imura, and H. Okamoto, "Time-resolved scanning near-field optical microscopy with supercontinuum light pulses generated in microstructure fiber," Rev. Sci. Instrum. **75**, 4528–4533 (2004).

[37]A. A. Mikhailovsky, M. A. Petruska, M. I. Stockman, and V. I. Klimov, "Broadband near-field interference spectroscopy of metal nanoparticles using a femtosecond white-light continuum," Opt. Lett. **28**, 1686–1688 (2003).

[38]R. M. Bakker, V. P. Drachev, H.-K. Yuan, and V. M. Shalaev, "Near-field, broadband optical spectroscopy of metamaterials," Physica B **394**, 137–140 (2007).

[39]P. Dvořák, Z. Édes, M. Kvapil, T. Šamořil, F. Ligmajer, M. Hrtoň, R. Kalousek, V. Křápek, P. Dub, J. Spousta, P. Varga, and T. Šikola, "Imaging of near-field interference patterns by aperture-type SNOM–influence of illumination wavelength and polarization state," Opt. Express **25**, 16560–16573 (2017).
[40]F. Keilmann and S. Amarie, "Mid-infrared frequency comb spanning an octave based on an Er fiber laser and difference-frequency generation," J. Infrared, Millimeter, Terahertz Waves **33**, 479–484 (2012).
[41]A. Gambetta, R. Ramponi, and M. Marangoni, "Mid-infrared optical combs from a compact amplified Er-doped fiber oscillator," Opt. Lett. **33**, 2671–2673 (2008).
[42]S. Amarie and F. Keilmann, "Broadband-infrared assessment of phonon resonance in scattering-type near-field microscopy," Phys. Rev. B **83**, 045404 (2011).
[43]E. Yoxall, M. Schnell, A. Y. Nikitin, O. Txoperena, A. Woessner, M. B. Lundeberg, F. Casanova, L. E. Hueso, F. H. L. Koppens, and R. Hillenbrand, "Direct observation of ultraslow hyperbolic polariton propagation with negative phase velocity," Nat. Photonics **9**, 674–678 (2015).
[44]S. Dai, Z. Fei, Q. Ma, A. S. Rodin, M. Wagner, A. S. McLeod, M. K. Liu, W. Gannett, W. Regan, K. Watanabe, T. Taniguchi, M. Thiemens, G. Dominguez, A. H. C. Neto, A. Zettl, F. Keilmann, P. Jarillo-Herrero, M. M. Fogler, and D. N. Basov, "Tunable phonon polaritons in atomically thin van der Waals crystals of boron nitride," Science **343**, 1125–1129 (2014).
[45]M. Eisele, T. L. Cocker, M. A. Huber, M. Plankl, L. Viti, D. Ercolani, L. Sorba, M. S. Vitiello, and R. Huber, "Ultrafast multi-terahertz nano-spectroscopy with sub-cycle temporal resolution," Nat. Photonics **8**, 841 (2014).
[46]F. J. Alfaro-Mozaz, P. Alonso-González, S. Vélez, I. Dolado, M. Autore, S. Mastel, F. Casanova, L. E. Hueso, P. Li, A. Y. Nikitin, and R. Hillenbrand, "Nanoimaging of resonating hyperbolic polaritons in linear boron nitride antennas," Nat. Commun. **8**, 15624 (2017).
[47]D. S. Shreesha Rao, R. D. Engelsholm, I. B. Gonzalo, B. Zhou, P. Bowen, P. M. Moselund, O. Bang, and M. Bache, "Ultra-low-noise supercontinuum generation with a flat near-zero normal dispersion fiber," Opt. Lett. **44**, 2216–2219 (2019).
[48]K. J. Kaltenecker, E. Krauss, L. Casses, M. Geisler, B. Hecht, N. A. Mortensen, P. U. Jepsen, and N. Stenger, "Mono-crystalline gold platelets: A high-quality platform for surface plasmon polaritons," Nanophotonics **9**, 509 (2020).
[49]F. Walla, M. M. Wiecha, N. Mecklenbeck, S. Beldi, F. Keilmann, M. D. Thomson, and H. G. Roskos, "Anisotropic excitation of surface plasmon polaritons on a metal film by a scattering-type scanning near-field microscope with a nonrotationally-symmetric probe tip," Nanophotonics **7**, 269–276 (2018).
[50]Z. Fei, A. S. Rodin, G. O. Andreev, W. Bao, A. S. McLeod, M. Wagner, L. M. Zhang, Z. Zhao, M. Thiemens, G. Dominguez, M. M. Fogler, A. H. C. Neto, C. N. Lau, F. Keilmann, and D. N. Basov, "Gate-tuning of graphene plasmons revealed by infrared nano-imaging," Nature **487**, 82–85 (2012).
[51]Y. Li, N. Zhou, E. C. Kinzel, X. Ren, and X. Xu, "The origin of interferometric effect involving surface plasmon polariton in scattering near-field scanning optical microscopy," Opt. Express **22**, 2965–2972 (2014).
[52]S. T. Sørensen, O. Bang, B. Wetzel, and J. M. Dudley, "Describing supercontinuum noise and rogue wave statistics using higher-order moments," Opt. Commun. **285**, 2451–2455 (2012).
[53]C. Lafargue, J. Bolger, G. Genty, F. Dias, J. M. Dudley, and B. J. Eggleton, "Direct detection of optical rogue wave energy statistics in supercontinuum generation," Electron. Lett. **45**, 217–219 (2009).
[54]R. Hillenbrand, B. Knoll, and F. Keilmann, "Pure optical contrast in scattering-type scanning near-field microscopy," J. Microsc. **202**, 77–83 (2001).
[55]K. M. McPeak, S. V. Jayanti, S. J. P. Kress, S. Meyer, S. Iotti, A. Rossinelli, and D. J. Norris, "Plasmonic films can easily be better: Rules and recipes," ACS Photonics **2**, 326–333 (2015).
[56]Z. M. Abd El-Fattah, V. Mkhitaryan, J. Brede, L. Fernández, C. Li, Q. Guo, A. Ghosh, A. R. Echarri, D. Naveh, F. Xia, J. E. Ortega, and F. J. García de Abajo, "Plasmonics in atomically thin crystalline silver films," ACS Nano **13**, 7771–7779 (2019).
[57]R. A. Maniyara, D. Rodrigo, R. Yu, J. Canet-Ferrer, D. S. Ghosh, R. Yongsunthon, D. E. Baker, A. Rezikyan, F. J. García de Abajo, and V. Pruneri, "Tunable plasmons in ultrathin metal films," Nat. Photonics **13**, 328–333 (2019).
[58]E. Genier, S. Grelet, R. D. Engelsholm, P. Bowen, P. M. Moselund, O. Bang, J. M. Dudley, and T. Sylvestre, "Ultra-flat, low-noise, and linearly polarized fiber supercontinuum source covering 670–1390 nm," Opt. Lett. **46**, 1820–1823 (2021).
[59]M. Pu, H. Hu, L. Ottaviano, E. Semenova, D. Vukovic, L. K. Oxenløwe, and K. Yvind, "Ultra-efficient and broadband nonlinear AlGaAs-on-insulator chip for low-power optical signal processing," Laser Photonics Rev. **12**, 1800111 (2018).
[60]Y. Yang, W. Wang, A. Boulesbaa, I. I. Kravchenko, D. P. Briggs, A. Puretzky, D. Geohegan, and J. Valentine, "Nonlinear Fano-resonant dielectric metasurfaces," Nano Lett. **15**, 7388–7393 (2015).
[61]J. Wang, S. Paesani, Y. Ding, R. Santagati, P. Skrzypczyk, A. Salavrakos, J. Tura, R. Augusiak, L. Mančinska, D. Bacco, D. Bonneau, J. W. Silverstone, Q. Gong, A. Acín, K. Rottwitt, L. K. Oxenløwe, J. L. O'Brien, A. Laing, and M. G. Thompson, "Multidimensional quantum entanglement with large-scale integrated optics," Science **360**, 285–291 (2018).